



## Effects of 1-methyl-2-pyrrolidinone (NMP) on polyamide-polysulfone TFC membrane pore morphology and ICP and membrane performance in forward osmosis

Yan Wu, Hongtao Zhu\*, Li Feng, Liqiu Zhang\*, Shanshan Xing

College of Environmental Science and Engineering, Beijing Forestry University, No. 35 Tsinghua East Road, Haidian District, Beijing, China, Tel. +86 18710116044; email: [wuyan5177@163.com](mailto:wuyan5177@163.com) (Y. Wu), Tel. +86 15910462326; email: [zhuhongtao@bifu.edu.cn](mailto:zhuhongtao@bifu.edu.cn) (H. Zhu), Tel. +86 15810056290; email: [fengli\\_hit@163.com](mailto:fengli_hit@163.com) (L. Feng), Tel. +86 15810056289; email: [zhangliqiu@163.com](mailto:zhangliqiu@163.com) (L. Zhang), Tel. +86 15210511051; email: [751571233@qq.com](mailto:751571233@qq.com) (S. Xing)

Received 30 December 2014; Accepted 23 March 2015

---

### ABSTRACT

In forward osmosis (FO), the influence of the pore morphology in the membrane support layer on membrane performance is still unclear. As a result, investigation into the relationship between membrane pore morphology and membrane performance in FO is meaningful. During the fabrication of a thin-film composite (TFC) FO membrane, the membrane pore morphology is related to the composition of the coagulant bath. In this study, varied concentrations (from 0 to 9 wt.%) of 1-methyl-2-pyrrolidinone (NMP) in a coagulant bath were applied to fabricate TFC FO membranes of different pore morphologies. The morphologies of the fabricated membranes were then characterized using FESEM, and the performance of each of the membranes was evaluated using a lab-scale FO setup. The FESEM images indicated that the increase in the NMP concentration elongated finger-like pores and suppressed the formation of large pores in the profile. When the NMP concentration was 9 wt.%, the finger-like pores nearly spanned the entire SL of the fabricated membrane. In addition, the open pores at the membrane bottom surface became smaller and fewer in number with the increase in the NMP concentration. The experimental FO results of the membranes indicated that internal concentration polarization reduction could be achieved by creating more long finger-like pores in the membrane SL as well as more and larger open pores at the membrane bottom surface. All of the fabricated membranes had a low rate of water flux ( $J_w$ ) to reverse salt flux ( $J_s$ ). In addition, the membrane fabricated with 3 wt.% NMP had the best performance in minimizing the draw solute loss, with a high  $J_w/J_s$  of 4.2 L/g.

*Keywords:* Forward osmosis; NMP; TFC FO membrane; Pore morphology; Coagulant bath

---

\*Corresponding authors.

*Presented at the 7th International Conference on Challenges in Environmental Science and Engineering (CESE 2014) 12–16 October 2014, Johor Bahru, Malaysia*

## 1. Introduction

Currently, the water resource crisis is an urgent global issue. In past decades, freshwater was produced from seawater or brackish water via desalination technologies, such as reverse osmosis, electrodialysis, and multi-stage flash, to satisfy daily water demand [1]. However, a large amount of energy is consumed in these desalination processes. In recent years, a novel desalination technology, forward osmosis (FO), has attracted increasing research interests [2,3].

In the FO process, a feed solution (FS) with low osmotic pressure and a draw solution (DS) with high osmotic pressure are separated by a semi-permeable membrane. Driven by the osmotic pressure difference across the membrane, pure water permeates the membrane from the FS to the DS. A water flux that can be recovered from the DS is then produced. In theory, a high water flux could be achieved via a high osmotic pressure difference. Thus, without applying hydraulic pressure, FO has good prospects in the fields of desalination and water treatment [4,5]. However, the actual water flux in FO is much lower than expected, which hinders the application of FO. Depending on the composition of the FS, the decrease in the membrane water flux is mainly due to membrane fouling and/or concentration polarization (CP). CP is a phenomenon in which the actual osmotic pressure difference across the membrane active layer is much lower than the theoretical osmotic pressure difference between the FS and DS bulks in FO. CP includes external concentration polarization (ECP) and internal concentration polarization (ICP) [6,7]. Generally, the FO membrane consists of a dense active layer (AL) and a porous support layer (SL). ECP occurs in solutions adjacent to the membrane surface, while ICP occurs within the membrane porous support layer. In the process of FO for which the membrane AL is facing the FS, the water flux dilutes the DS in the porous membrane SL, resulting in a significant osmotic pressure drop in the membrane SL. This is the so-called dilutive internal concentration polarization (DICP), which leads to a drastic decrease in the actual osmotic pressure difference across the membrane AL and results in a lower water flux than predicted [8,9]. DICP is dependent on the membrane SL structure and properties, such as thickness, tortuosity, hydrophobicity, and porosity [10,11]. Therefore, many researchers have focused on the study of the optimization of the FO membrane to enhance the water flux.

In the past two decades, the only commercial membranes for FO applications have been made from cellulose triacetate (CTA) or cellulose acetate (CA) by

Hydration Technology Innovations, LLC (HTI). However, the use of these CTA & CA membranes in desalination have been limited because of their relatively low pure water permeability, salt rejection, and poor chemical stability in the  $\text{NH}_4\text{HCO}_3$  DS [12]. Thus, Yip et al. [12] fabricated thin-film composite (TFC) FO membranes via phase inversion and interfacial polymerization in 2010. The membranes that they produced were thinner, more porous, more chemically stable to the  $\text{NH}_4\text{HCO}_3$  DS, and performed better than HTI membranes in lab-scale FO experiments. In recent years, TFC FO membranes have gained more attention compared with cellulose acetate FO membranes. Researchers have conducted many studies on the optimization of the TFC membrane active layer [13–18] and support layer [19–26] or on the mathematical modeling of membrane mass transfer [27–30]. HTI also developed a commercial TFC membrane that performed well in the FO process, according to the results in the study of Ren and McCutcheon [31]. As DICP and the FO water flux are related to the structure of the TFC FO membrane SL, studying the relationships among the membrane SL structure, DICP, and membrane performance in FO would benefit FO membrane optimization and FO application.

Generally, the TFC FO membrane AL is fabricated via interfacial polymerization, and the membrane SL is fabricated via phase inversion [12,32]. To obtain a porous membrane SL with different structures, immersion precipitation is a commonly used method. In immersion precipitation, the prepared membrane casting solution is immersed into a non-solvent coagulant bath to form the porous membrane SL via phase inversion. During this process, the composition of the coagulant bath plays a key role in membrane pore formation.

Studies indicated that adding solvent, e.g., 1-methyl-2-pyrrolidinone (NMP), into the coagulant bath could influence the pore morphology in the membrane [33]. This influence is related to the membrane pore morphology being determined by the liquid–liquid demixing types during phase inversion. Instantaneous demixing tends to form macrovoids, which includes finger-like and large pore morphology, while a delayed demixing may induce the formation of sponge-like pores in the membrane SL. The addition of solvent to the coagulation bath lowers the non-solvent activity and diffusion rate into the polymer film, which would further delay demixing and result in pore morphology changes in the membrane SL [33].

ICP can be decided by the membrane SL structure (i.e. pore morphology); therefore, the composition of the coagulant bath may further influence the membrane performance in FO by affecting the SL

structures. Based on this point, studying the inter-relationship between the coagulant bath composition, membrane structure, and membrane FO performance is meaningful to FO membrane optimization as well as to FO industrial application.

In this study, a series of TFC FO membrane SLs were fabricated using coagulant baths with varied NMP concentrations from 0 to 9 wt.%. The AL of all of the TFC FO membranes was fabricated via interfacial polymerization under the same conditions. The effects of the NMP concentrations in the coagulant bath on the TFC FO membrane SL structure and the effects of membrane SL structure on ICP and membrane FO performances were systematically investigated with the results of membrane characterizations and experimental FO performances. The findings of this work may help to provide further understanding on how to optimize TFC FO membrane structure.

## 2. Materials and methods

### 2.1. Materials

Polysulfone beads (Mn ~22,000, Sigma Aldrich), 1-methyl-2-pyrrolidinone (NMP, anhydrous, 99.5%, Sigma Aldrich), N,N-dimethylformamide (DMF, anhydrous, 99.8%, Sigma Aldrich) were used to fabricate the porous polysulfone support layer of membrane. 1,3-phenylenediamine (MPD, >99%, Sigma-Aldrich), 1,3,5-benzenetricarbonyltrichloride (TMC, 98%, Sigma Aldrich), an organic solvent Isopar-G (Exxon Mobil, China) were used to fabricate the dense polyamide active layer of membrane. Sodium chloride (NaCl, ≥99.5%, Sinopharm Chemical Reagent) and deionized (DI) water were used to test the membrane performance in FO experiments.

### 2.2. Fabrication of TFC FO membrane

#### 2.2.1. Fabrication of the membrane polysulfone support layer

Psf beads dried overnight were dissolved into a composite solvent of DMF and NMP to prepare the

membrane casting solution. Before being casted onto a clean glass plate with a casting knife at a 100- $\mu$ m thickness, the membrane casting solution was stirred for at least 8 h and degassed overnight. Immediately after casting, the thin as-cast liquid films were immersed into coagulant baths with varied NMP concentrations of 0, 3, 6, and 9 wt.% at room temperature. After 10 min, the membrane support layers formed in the coagulant bath were thoroughly washed with DI water and then kept in DI water until the formation of polyamide. The composite recipes of the casting solution and coagulant bath are presented in Table 1.

#### 2.2.2. Fabrication of the membrane polyamide active layer

The polyamide active layer was fabricated via the interfacial polymerization of MPD dissolved in the liquid phase solution and TMC dissolved in the organic phase solution using the unified method. First, the membrane polysulfone support layers were immersed in a 3.4 wt.% MPD aqueous solution for 120 s. After removing liquid drops on the surface, the top surfaces of the MPD saturated membrane support layers were allowed to be in contact with 0.15 wt.% TMC in Isopar-G for 60 s. Next, the fabricated TFC FO membranes were thoroughly rinsed by DI and stored for further use.

### 2.3. Characterization of the TFC FO membrane

#### 2.3.1. Measurement of the membrane thickness and hydrophilicity

The thickness ( $t_s$ ) of the membrane support layers was measured using a digital micrometer (series 293-240, Mitutoyo, Guangdong, China). For each membrane SL sample, the value of  $t_s$  was measured 10 times at 10 different locations. The contact angle (CA) of the membranes was measured using a contact angle goniometer (OCA20, Dataphysics,

Table 1

Composite recipes of the membrane casting solution and the coagulant bath

Membrane	Casting solution composition			Coagulant bath composition	
	Psf (wt.%)	NMP (wt.%)	DMF (wt.%)	NMP (wt.%)	DI (wt.%)
M <sub>0</sub>	12	22	66	0	100
M <sub>3</sub>	12	22	66	3	97
M <sub>6</sub>	12	22	66	6	94
M <sub>9</sub>	12	22	66	9	91

Germany). For each membrane sample, CA was measured at 20 different locations and averaged. Before the measurements, all of the samples were dried overnight in a desiccator.

### 2.3.2. Characterization of the membrane structural morphology

The surface and cross-sectional morphology of the membrane samples were characterized by a field-emission scanning electron microscope (FESEM, S-3400N, Hitachi) after being coated with platinum using an ion sputter (E-1010, Hitachi). In addition, the diameter ( $d$ ) of the open pores at the membrane bottom surface was measured using the FESEM measurement software. For each membrane sample, the average open pore diameter at the membrane bottom surface was measured and calculated based on 100 random pores. Meanwhile, the total areas of open pores in the unit area of the membrane surface were determined by image processing software (ImageJ, National Institute of Mental Health, USA) for each sample. The proportion of the open pore area in the total membrane surface area was calculated and summarized. Before characterization, all of the samples were freeze-fractured in liquid nitrogen and then dried in a desiccator for 24 h.

### 2.3.3. Determination of the membrane support layer porosity

The dried membrane support layer samples were weighed using an analytical balance (AL 204, Mettler Toledo), and the porosity ( $\varepsilon$ ) of the membrane support layer samples was calculated by the following equation:

$$\varepsilon (\%) = \frac{\rho \cdot S_m \cdot t_s - W_s}{(\rho - \rho_i) \cdot S_m \cdot t_s} \times 100 \quad (1)$$

where  $\rho$  is the density of Psf ( $1.25 \times 10^3 \text{ kg/m}^3$ ) and  $S_m$  and  $t_s$  are the area and thickness of the sample, respectively.  $W_s$  is the weight of the membrane support layer sample, and  $\rho_i$  is the density of air ( $1.20 \text{ kg/m}^3$ ) under the testing condition. The principle of the  $\varepsilon$  measurement method in this work is the same as the principle of testing the membrane weight change before and after being dried, as described by Emadzadeh et al. [32].

### 2.4. Evaluation of the membrane intrinsic water permeability and solute rejection

The intrinsic water permeability and solute rejection of TFC FO membranes fabricated in this work were evaluated using a dead-end ultrafiltration (UF) setup. The membrane pure water permeability ( $A$ ) was tested in the UF setup at an applied trans-membrane pressure of 3.5 bar using DI water as a FS. When the water steadily permeated the membrane,  $A$  was determined by measuring the volume of permeate water and then calculated using the following Eq. (2):

$$A = \frac{\Delta V_m}{S_m \cdot P \cdot \Delta t} \quad (2)$$

where  $\Delta V_m$  is the volume of the water that permeated the membrane,  $S_m$  is the effective membrane area in the UF setup,  $P$  is the impressed pressure across the membrane, and  $\Delta t$  is the time during which water permeated the membrane.

The membrane salt rejection,  $R$ , was also tested in the UF setup with 50 mM NaCl as the FS. In the test, the FS was stirred by a paddle to circularly flow in the horizontal direction in the setup while the water permeated in the vertical direction. To calculate  $R$ , the following equation was used:

$$R = \left(1 - \frac{C_p}{C_f}\right) \times 100 \quad (3)$$

where  $C_p$  and  $C_f$  are the salt concentrations in the permeating solution and FS, respectively. Based on the solution-diffusion theory, the solute permeability coefficient ( $B$ ) of membrane was calculated by:

$$\frac{1 - R}{R} = \frac{B}{A \cdot (\Delta P - \Delta \pi)} \quad (4)$$

where  $A$  is the pure water permeability,  $\Delta P$  is the pressure difference, and  $\Delta \pi$  is the osmotic pressure difference across the membrane.

### 2.5. Evaluation of the membrane FO performance

The experimental performances of the TFC FO membranes fabricated in this work were evaluated using a lab-scale FO setup. In our experiments, all of the tests were performed at room temperature ( $25 \pm 1^\circ\text{C}$ ) in FO mode, for which the membrane active layer was facing the FS and the support layer to the

DS. The effective membrane area in the setup was 30 cm<sup>2</sup>. During the FO test, the FS and the DS were pumped to flow in parallel. Both FS and DS were circulated at a fixed flow rate of 22 cm/s on the membrane top and bottom surfaces. The DS used in the experiments was NaCl aqueous solution of varied concentration of 0.5, 1.0, 1.5, and 2.0 M. The FS was DI water. The experimental membrane water flux ( $J_w$ ) in FO was determined by measuring the weight changes of the FS using a digital balance (Mettler Toledo, PL2002) linked to a computer. The experimental membrane reverse salt flux ( $J_s$ ) was determined by measuring the salt concentration in the FS using a conductivity meter.

### 2.6. Determination of the membrane structural parameters

According to the mass transfer theory in the FO process [10,23], the resistance to solute diffusion,  $K$ , was calculated using the following equation:

$$K = \frac{1}{J_w} \cdot \ln \frac{B + A \cdot \pi_{D,b}}{B + J_w + A \cdot \pi_{F,m}} \quad (5)$$

where  $J_w$  is the experimental water flux in FO.  $B$  and  $A$  are the solute permeability and the water permeability of membrane, respectively.  $\pi_{D,b}$  is the bulk osmotic pressure of the DS, and  $\pi_{F,m}$  is the osmotic pressure at the membrane surface on the feed side (0 bar for DI water). The resistance  $K$  could also be expressed as the reciprocal of a thin-film mass transfer coefficient:

$$K = \frac{t_s \cdot \tau}{D \cdot \varepsilon} \quad (6)$$

where  $t_s$  is the support layer thickness,  $\tau$  is the tortuosity,  $D$  is the diffusion coefficient of the draw solute, and  $\varepsilon$  is the porosity.

The membrane structural parameter,  $S$ , which is independent of the DS properties, assuming the draw solutes do not swell or plasticize the Psf support layer [12], was defined as:

$$S = K \cdot D = \frac{t_s \cdot \tau}{\varepsilon} \quad (7)$$

Basically, an ideal TFC FO membrane should have a low  $S$  value, which is the indicator for ICP in the membrane in the FO process. In FO process, milder ICP is due to smaller  $S$  values of membranes employed [34].

## 3. Results and discussion

### 3.1. Effects of the NMP concentration in the coagulant bath on the physiochemical properties of the fabricated membranes

The physiochemical properties of the membranes fabricated in this work are summarized in Table 2. No significant differences were found in properties such as thickness, porosity, and contact angle (approximately 82.4–85.9° for four membranes) among the different membranes. This result indicates that the variation of the NMP concentration in the coagulant bath has no evident effect on the membrane physiochemical properties. Generally speaking, when the casting knife gate is fixed at a constant height, the thickness and contact angle of the membranes are then largely controlled by the composition of the membrane casting solution. In this work, the casting solutions were prepared using the same method, this might be the reason why there is no significant difference in membrane thickness and hydrophilicity observed.

### 3.2. Effects of the NMP concentration in the coagulant bath on the structural morphology of the fabricated membranes

Fig. 1 shows SEM images of the cross-sections and the bottom surfaces of the membranes fabricated in this work. These images indicate the different structural morphologies of the membranes fabricated for different NMP concentrations.

From the cross-sectional images in Fig. 1, although the pore distributions were distinct in different

Table 2  
Thickness, contact angle, and porosity of membranes fabricated using different NMP concentrations in the coagulant bath

Membrane	Thickness, $t_s$ ( $\mu\text{m}$ )	Contact angle, CA ( $^\circ$ )	Porosity, $\varepsilon$ (%)
M <sub>0</sub>	51.1 ± 2.0	84.2 ± 1.6	82.3 ± 0.2
M <sub>3</sub>	52.0 ± 1.6	83.8 ± 1.5	83.7 ± 0.1
M <sub>6</sub>	50.4 ± 1.8	85.9 ± 1.2	84.0 ± 0.3
M <sub>9</sub>	51.6 ± 1.2	82.4 ± 2.0	83.8 ± 0.1

membranes, the support layers of all four membranes consist of sponge-like pores, finger-like pores, and large-pores (the macrovoids that do not have a finger-like morphology). For all four membranes, the top parts of their support layers were filled with sponge-like pores with diameters of less than 20 nm. The morphologies of the macrovoids located under the sponge-like top layers were observed to be much different in the fabricated membranes. When the NMP concentration in the coagulant bath was increased from 0 to 6 wt.%, the macrovoids in the membrane appeared in both finger-like pores and large pores (Fig. 1(a)–(c)). However, when the concentration of NMP reached 9 wt.%, the large pores disappeared in the membrane SL, and the finger-like pores spanned the entire support layer, from the bottom of sponge top layer to the membrane bottom surface (Fig. 1(d)). In addition, the large pores near the bottom of membrane M<sub>0</sub>, M<sub>3</sub>, and M<sub>6</sub> were surrounded by sponge-like pore layer walls.

In addition to the pore morphology, the portions of macrovoids taken into the membrane cross-sections were quite different. With the increase in the NMP concentrations in the coagulant bath from 3 to 9 wt.%, the proportions of large pores in the entire cross-sections of the membranes decreased, while the proportions of finger-like pores gradually increased. Meanwhile, the width of the large pore (i.e. in the direction parallel to the membrane surface) exhibited a gradual decrease.

The cross-sectional pore morphology of the membranes fabricated in this work was directly related to the addition of NMP. The increase in the NMP concentration in the coagulant bath from 0 to 9 wt.% decreases the non-solvent (i.e. DI water) diffusion rate into the polymer film and further delays the demixing process. Delayed demixing causes (at least a part of) the macrovoids in membrane SL to form a finger-like morphology instead of large pores. As a result, the formation of large pores is suppressed.

From the membrane bottom surface images in Fig. 1, the size and number of open pores at different membrane bottom surfaces are observed to vary with each other. As the NMP concentration increases from 0 to 9 wt.%, both the size and the number of open pores per unit surface area obviously decreased. In particular, membrane M<sub>9</sub>, which features finger-like pores spanning the entire support layer (Fig. 1(d)), had relatively smaller and less open pores at the membrane surface when compared with the other membranes (Fig. 1(h)).

For further analysis, the diameters ( $d$ ) of 100 bottom surface open pores observed in SEM images were measured using the FESEM measurement software and averaged. In addition, the total areas of the open

pores per unit area of the membrane surface were measured using Image J, and the percentages of the open pore area taken per unit membrane surface area were then calculated and summarized. Table 3 presents the open pore diameters and the area percentages of the membranes fabricated in this work. As the NMP concentration increased from 0 to 6 wt.%, both the diameter and the percentage of open pore area sharply decreased, whereas the size and the percentage of open pore area slightly decreased ( $49.2 \pm 3.1 \mu\text{m}$  and  $5.21 \pm 0.19\%$  for M<sub>6</sub>, by contrast  $53.2 \pm 2.9 \mu\text{m}$  and  $4.22 \pm 0.48\%$  for M<sub>9</sub>) when the NMP concentration varied from 6 to 9 wt.%.

In the membranes fabricated in this work, membranes M<sub>0</sub>, M<sub>3</sub>, and M<sub>6</sub> contained large pores, whereas membrane M<sub>9</sub> featured no large pores, but instead exhibited finger-like pores that spanned the entire membrane. In addition, M<sub>6</sub> and M<sub>9</sub> exhibited fewer and smaller open pores at the membrane surfaces compared to the other membranes. The obvious membrane structure difference resulting from the variation of NMP concentration may lead to different membrane performances in FO. The relationship between the membrane structure and the membrane performance reflects the severity of ICP and the effects of different pore morphologies on ICP.

### 3.3. Effects of SL structure on the membrane permeable properties

Table 4 shows the obtained water permeability  $A$ , salt rejection  $R$ , solute permeability coefficient  $B$ , and structural parameter  $S$  of the membranes fabricated using different NMP concentrations. The salt rejection  $R$  values of the four fabricated TFC membranes were all found to be at the same level. With the increase in the NMP concentration from 0 to 9 wt.% in the coagulant bath, the salt rejection  $R$  of the membranes slightly fluctuated between 94.8 and 95.2%, while the pure water permeability  $A$  increased from 0.99 to  $1.13 \text{ L m}^{-2} \text{ h}^{-1} \text{ bar}^{-1}$ . According to the water permeating principle in FO [35], the theoretical water flux ( $J_w^t$ ) of membranes can be calculated using Eq. (8):

$$J_w^t = A \cdot \Delta\pi \quad (8)$$

where  $A$  is the pure water permeability and  $\Delta\pi$  is the apparent osmotic pressure difference across membrane. This equation indicates that when provided with the same  $\Delta\pi$ , the theoretical FO water flux of the fabricated membranes should also increase gradually with pure water permeability.

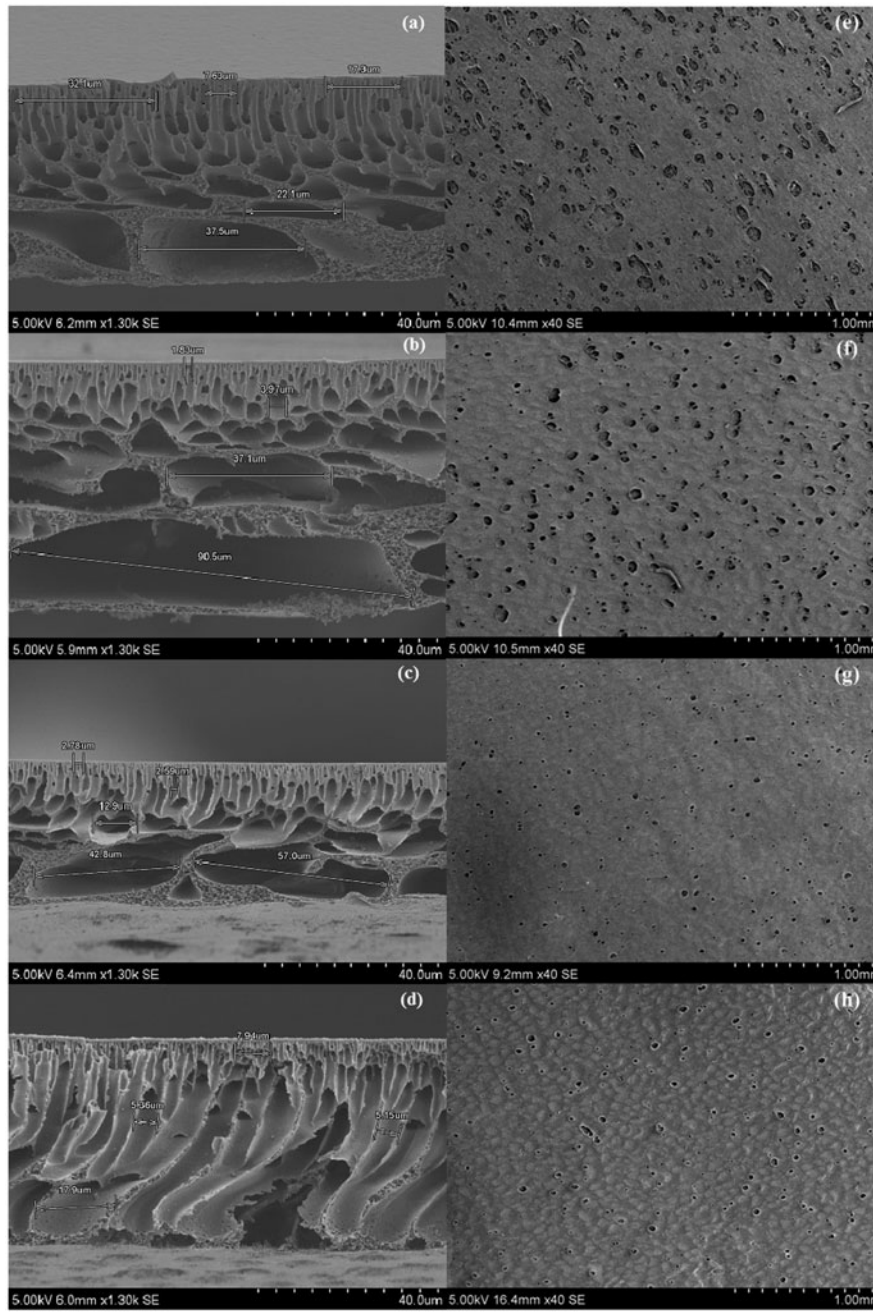


Fig. 1. Typical SEM images of membranes fabricated with different NMP concentrations in coagulant bath. Membrane cross-section images: (a)  $M_0$ ; (b)  $M_3$ ; (c)  $M_6$ ; and (d)  $M_9$ . Membrane bottom surface images: (e)  $M_0$ ; (f)  $M_3$ ; (g)  $M_6$ ; and (h)  $M_9$ .

The structural parameter ( $S$ ) indirectly reflects the severity of ICP in the membrane in the FO process, as previously mentioned in this paper. Generally, membranes with small  $S$  values have low ICP. As presented in Table 4, the descending sequence of the membrane structural parameters was determined to be:  $S(M_6) > S(M_0) > S(M_9) > S(M_3)$ . As per Table 4,

it can be concluded that membrane  $M_9$  and  $M_6$ , both of which had smaller and less bottom surface open pores but different pore morphologies in the support layer profile, had different  $S$  values (305  $\mu\text{m}$  for  $M_9$  and 530  $\mu\text{m}$  for  $M_6$ ). This result indicates that more finger-like pores, especially pores spanning the entire support layer, may contribute to membrane ICP

Table 3

Diameter ( $d$ ) and area percentage of the open pores at the bottom surface of the membranes fabricated using different NMP concentrations in the coagulant bath

Membrane	Pore diameter, $d$ ( $\mu\text{m}$ )	Pore area percentage (%)
M <sub>0</sub>	94.6 ± 4.2	18.33 ± 0.53
M <sub>3</sub>	88.3 ± 2.8	16.07 ± 0.97
M <sub>6</sub>	49.2 ± 3.1	5.21 ± 0.19
M <sub>9</sub>	53.2 ± 2.9	4.22 ± 0.48

reduction, despite the effects of the open pores at the membrane bottom surface. The reason for this ICP reduction may be that, compared to finger-like pores, the sponge-like pores and large pores in the membrane support layer increased the resistance to mass transfer during the FO process. In FO, ICP results from the lower DS concentration in the membrane support layer. Compared with the large pores and sponge-like pores with relatively higher  $\tau$ , the finger-like pores provided the permeated water a short path to the bulk DS. This process may allow DS concentrations to increase in the membrane SL and in the bulk DS to achieve equilibrium in a short time span.

Meanwhile, although membranes M<sub>0</sub>, M<sub>3</sub>, and M<sub>6</sub> have mixed structural morphologies of sponge-like pores and large pores in the support layers, they exhibited quite different  $A$  and  $S$  values. Compared to membrane M<sub>0</sub>, the sizes of the large pores in M<sub>3</sub> were much larger, while the diameters and area percentages of the open pores at the bottom surface of M<sub>3</sub> were slightly reduced. The higher water permeability ( $1.08 \text{ L m}^{-2} \text{ h}^{-1} \text{ bar}^{-1}$ ) and lower  $S$  value ( $220 \mu\text{m}$ ) of M<sub>3</sub> indicated that for the large pores in the membrane SL, a larger size could contribute to the reduction of membrane mass transfer resistance and ICP in FO. Both membranes M<sub>0</sub> and M<sub>6</sub> have different appearances of open pore diameters and areas at the bottom surface. Membrane M<sub>6</sub>, the bottom surface

open pores of which were much fewer in number and smaller, had the highest  $S$  value ( $530 \mu\text{m}$ ) of the membranes studied. This result indicated that the presence of a large number of open pores at the membrane bottom surface reduces the severity of ICP.

Therefore, based upon the results of this work, an ideal TFC FO membrane should feature finger-like pores in the SL profile as well as a greater number of large open pores at the membrane bottom surface.

### 3.4. Effects of the membrane SL structure on ICP and membrane water flux in FO

In this study, the performance of the membranes fabricated using different NMP concentrations was evaluated in a designed lab-scale FO setup. Before the experimental values of the water flux ( $J_w$ ) and experimental reverse salt flux ( $J_s$ ) of membranes are measured, the FO setup was allowed to run for three hours to ensure that ICP had completely formed. For each membrane, the water flux under different DS concentrations was measured 3 times and averaged. In addition, DI water was used as the FS to avoid membrane fouling, and DS and FS were both pumped to flow at a high speed ( $22 \text{ cm/s}$ ) on the membrane surfaces to diminish the ECP effects.

The calculated theoretical water fluxes ( $J_w^t$ ) and the obtained experimental water fluxes ( $J_w$ ) of the membranes fabricated in this work are presented in Figs. 2 and 3, respectively. As shown in Figs. 2 and 3, the values of  $J_w$  were much lower than the values of  $J_w^t$  for all four fabricated membranes, e.g. for membrane M<sub>9</sub>,  $J_w^t$  was  $134.3 \text{ L m}^{-2} \text{ h}^{-1}$  (LMH), while  $J_w$  was only  $23.8 \text{ LMH}$  when using  $2.0 \text{ M NaCl}$  as the DS. As mentioned above, the effects of membrane fouling and ECP could be ignored in the FO experiments; thus, the difference between  $J_w^t$  and  $J_w$  could be attributed to ICP only. In addition, note that the descending sequence of membrane theoretical water flux was  $J_w^t(\text{M}_0) > J_w^t(\text{M}_6) > J_w^t$

Table 4

Pure water permeability, salt rejection, solute permeability coefficient, and structural parameter of the membranes fabricated using different NMP concentrations in the coagulant bath

Membrane	Pure water permeability, $A$ ( $\text{L m}^{-2} \text{ h}^{-1} \text{ bar}^{-1}$ )	Salt rejection, $R$ (%)	Solute permeability coefficient, $B$ ( $\text{L m}^{-2} \text{ h}^{-1}$ )	Structural parameter, $S$ ( $\mu\text{m}$ )
M <sub>0</sub>	0.99	95.10	1.54	341
M <sub>3</sub>	1.08	95.20	1.66	220
M <sub>6</sub>	1.09	94.90	1.78	530
M <sub>9</sub>	1.13	94.80	1.87	305

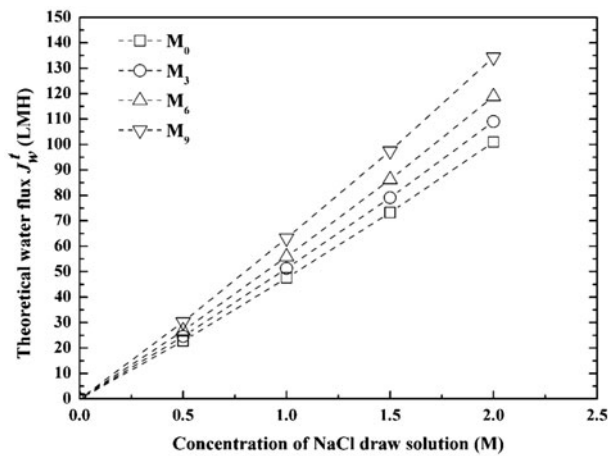


Fig. 2. Theoretical water flux of membranes fabricated with different NMP concentrations in coagulant bath.

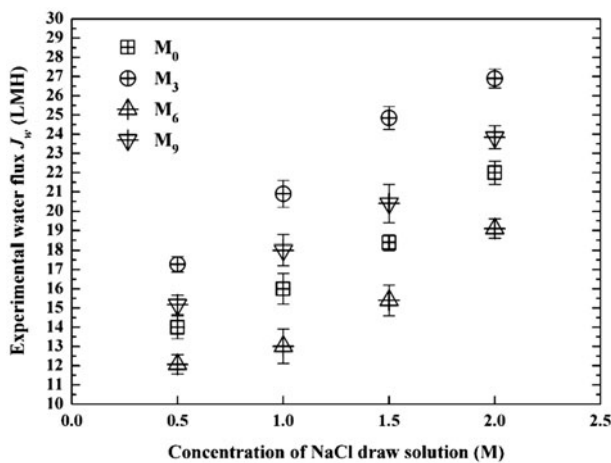


Fig. 3. Experimental water flux of membranes fabricated with different NMP concentrations in coagulant bath.

( $M_3$ ) >  $J_w^t$  ( $M_0$ ) (shown in Fig. 2), while the experimental water flux descending sequence followed the order of  $J_w$  ( $M_3$ ) >  $J_w$  ( $M_9$ ) >  $J_w$  ( $M_0$ ) >  $J_w$  ( $M_6$ ), as shown in Fig. 3. In the process of FO, the actual membrane water flux was determined by the effective osmotic pressure difference ( $\Delta\pi_{eff}$ ) across the TFC FO membrane AL. The theoretical membrane water flux was calculated assuming that  $\Delta\pi_{eff}$  is equal to  $\Delta\pi$  provided by the bulk FS and DS. In fact, the sum of the osmotic pressure difference reduced by ICP and  $\Delta\pi_{eff}$  is assumed to be equal to  $\Delta\pi$ . Therefore, the distinction of the two water flux sequences is attributed to the differences in the ICP severity, which was influenced by the membrane SL structures.

Fig. 4 shows the difference between  $J_w^t$  and  $J_w$  for each fabricated membrane. From Fig. 4, for one mem-

brane, the difference between  $J_w^t$  and  $J_w$  is observed to change with the variation of the DS concentration. Under the same DS concentration, the differences among the membranes were distinct under different NMP concentrations.

For further analysis, the rate of water flux reduced in FO to the theoretical water flux ( $r$ , %) was calculated using Eq. (9) in this study,

$$r (\%) = \frac{J_w^t - J_w}{J_w^t} \times 100 \quad (9)$$

where  $J_w^t$  and  $J_w$  are the theoretical water flux and the experimental water flux of membrane, respectively. Similar to the  $S$  value, the  $r$  value would alternatively reflect the severity of ICP in membranes.

Fig. 5 shows the  $r$  values of different membranes under various DS concentrations. From Fig. 5, the  $r$  values range between 30 and 85%. For each membrane, the  $r$  values exhibit a non-linear increasing trend with the increase in the DS concentration. This result indicated that for each membrane, the DS concentration is directly proportional to both the ICP severity and the water flux reduction. Meanwhile, the comparison of the  $r$  values between different membranes revealed a descending sequence of  $r$  ( $M_6$ ) >  $r$  ( $M_9$ ) >  $r$  ( $M_0$ ) >  $r$  ( $M_3$ ), e.g. when using 1.0 M NaCl as the DS, the percentages of water flux reduced in FO were 66.3, 59.3, 76.7, and 71.5% for membranes  $M_0$ ,  $M_3$ ,  $M_6$ , and  $M_9$ , respectively. The results of membrane  $M_6$  and  $M_9$  shown in Fig. 5 also indicated that finger-like pores in membrane SL might contribute to ICP reduction.

However, in this study, the water producing ability of membrane  $M_3$  with mixed structural morphologies, instead of membrane  $M_9$  with only finger-like pores, was preferred. The reduction of ICP in membrane  $M_3$  is probably due to the large open pores at the membrane bottom surface, which would assist solutes in bulk DS to transfer into the membrane SL, thereby reducing ICP. This result indicates that ICP was simultaneously influenced by the membrane SL structure morphology and the size and area of bottom surface open pores. In this study, the effects of open pores at membrane bottom surface may have a more significant impact on ICP reduction than that due to the membrane SL structural morphology.

### 3.5. Effects of the SL structure on the reverse salt flux in FO

Fig. 6 shows the reverse salt flux ( $J_s$ ) of membranes fabricated using different NMP concentrations. From

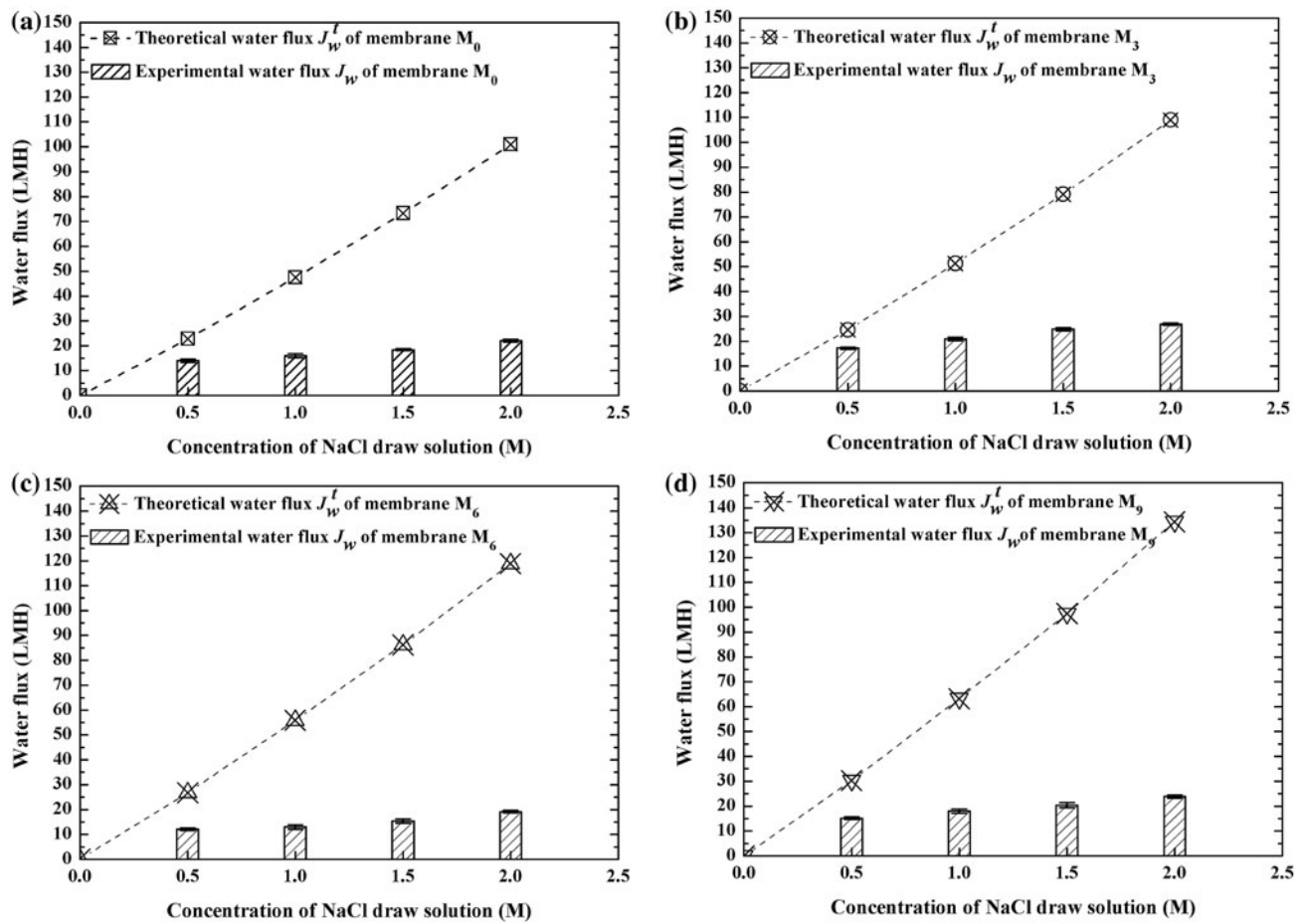


Fig. 4. Comparison of theoretical water flux and experimental water flux of membranes fabricated with different NMP concentrations in coagulant bath: (a–d) are for membranes M<sub>0</sub>, M<sub>3</sub>, M<sub>6</sub>, and M<sub>9</sub>, respectively.

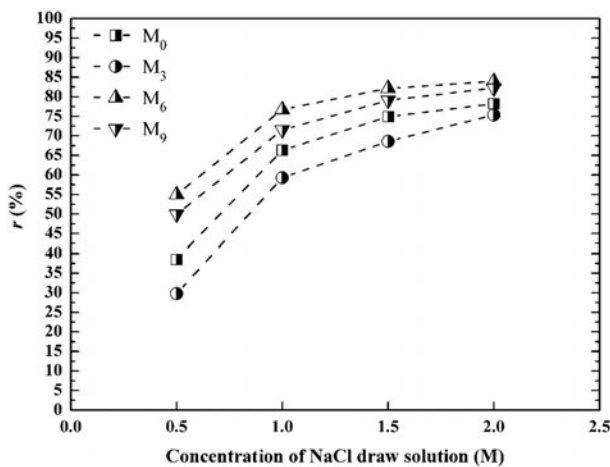


Fig. 5. Rate of water flux reduced in FO to membrane theoretical water flux under different DS concentrations. The higher the  $r$  value is, the more severe ICP in membrane is.

Fig. 6, the reverse salt fluxes of all of the fabricated membranes did not exceed 6 g MH, reflecting the profound abilities of PA–Psf TFC FO membranes in the retention of the solute in the DS. For each membrane, the reverse salt flux of the membrane increased with the DS concentration. In addition, the reverse salt flux exhibited a descending order of  $J_s$  (M<sub>3</sub>) >  $J_s$  (M<sub>9</sub>) >  $J_s$  (M<sub>0</sub>) >  $J_s$  (M<sub>6</sub>), which is in agreement with the membrane experimental water flux ranking.

The rate of water flux to reverse salt flux,  $J_w/J_s$ , reflects the ability of the FO membrane in minimizing the loss of the draw solute, as a high  $J_w/J_s$  ratio denotes minimum adverse effects of draw solute loss [36]. Fig. 7 shows the  $J_w/J_s$  of membranes fabricated using different NMP concentrations in this work. It can be concluded from Fig. 7 that membrane M<sub>3</sub> had the highest value of  $J_w/J_s$ , while M<sub>9</sub> had the lowest.

Therefore, the fabricated membrane using the NMP concentration of 3 wt.% exhibited the lowest ICP and had the highest ability to minimize draw solute loss.

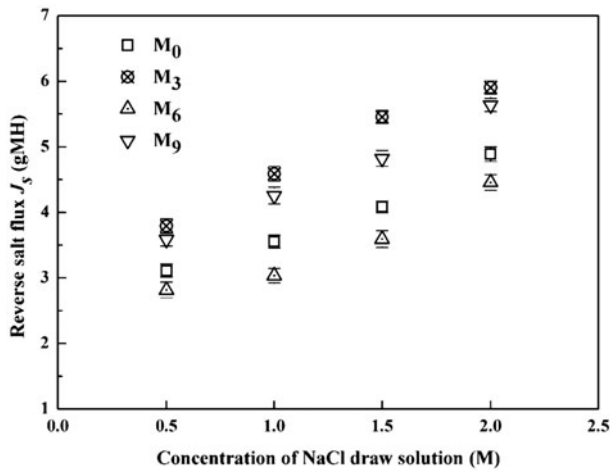


Fig. 6. Experimental reverse salt flux of membranes fabricated with different NMP concentrations in coagulant bath.

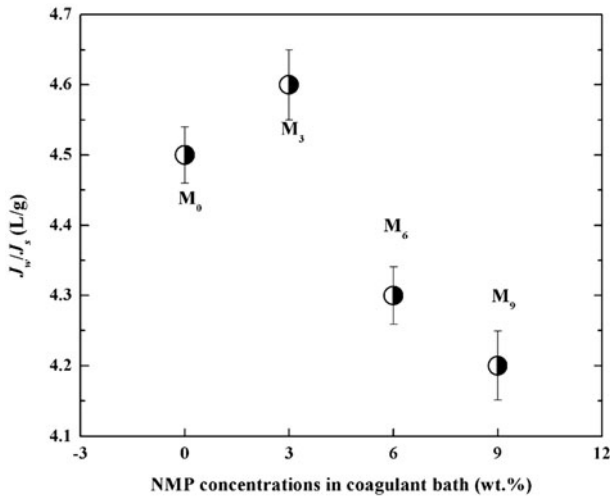


Fig. 7. Rate of experimental water flux ( $J_w$ ) to experimental reverse salt flux ( $J_s$ ) of membranes fabricated with different NMP concentrations in coagulant bath.

#### 4. Conclusions

This work investigated the effects of the NMP concentration in the coagulant bath on the PA–Psf TFC FO membrane structure and the membrane performances in FO. According to the experimental results, the following conclusions can be drawn:

- (1) The variation of the NMP concentration in the coagulant bath had obvious effects on the membrane structural morphology during immersion precipitation. The increase in the NMP concentration in the coagulant bath delayed the demixing process, leading to a reduction of large pores and an increase in fin-

ger-like pores in the profile. In particular, when the NMP concentration was 9 wt.%, the finger-like pores in the membrane SL spanned nearly the entire membrane SL. Meanwhile, the size and number of open pores at the membrane bottom surface tended to decrease with the addition of NMP.

- (2) Both the pore profile morphology in the membrane SL and the open pores at the bottom surface influenced ICP. For the TFC FO membrane, higher numbers and longer finger-like pores in the membrane SL contributed to ICP reduction, while a decrease in the diameter and the open pore area per unit membrane bottom surface can increase the severity of ICP. Therefore, an ideal TFC FO membrane features a support layer with wide finger-like pores as well as higher number and larger open pores at the bottom surface.
- (3) In this work, the fabricated PA–Psf TFC FO membranes had relatively high values of  $J_w/J_s$ . Among all of the membranes, the one fabricated using 3 wt.% NMP in the coagulant bath exhibited the highest  $J_w/J_s$ , indicating its high ability to minimize draw solute loss in FO.

#### Acknowledgements

The authors acknowledge the financial support from the Fundamental Research Funds for the Central Universities (No. TD2011-24, TD-JC-2013-3), the National Natural Science Foundation of China (51208037), and the Special S&T Project on Treatment and Control of Water Pollution (2013ZX07201007-003).

#### List of symbols

$J_w$	— experimental water flux ( $\text{L m}^{-2} \text{h}^{-1}$ )
$J_s$	— experimental reverse salt flux ( $\text{g m}^{-2} \text{h}^{-1}$ )
$\varepsilon$	— membrane porosity (%)
$W_s$	— weight of the dry membrane (g)
$\rho$	— density of polysulfone ( $\text{kg m}^{-3}$ )
$\rho_i$	— density of air ( $\text{kg m}^{-3}$ )
$\rho_w$	— density of the water permeated ( $\text{kg m}^{-3}$ )
$\Delta t$	— permeating time of water (s)
$S_m$	— membrane area ( $\text{cm}^2$ )
$t_s$	— membrane thickness ( $\mu\text{m}$ )
$A$	— pure water permeability ( $\text{L m}^{-2} \text{h}^{-1} \text{bar}^{-1}$ )
$A_m$	— effective membrane area in ultrafiltration ( $\text{m}^2$ )
$\Delta W$	— weight of the water permeated (L)
$p$	— pressure (bar)
$R$	— salt rejection (%)
$C_f$	— feed concentration ( $\text{mol L}^{-1}$ )
$C_p$	— permeate concentration ( $\text{mol L}^{-1}$ )
$B$	— solute permeability coefficient ( $\text{L m}^{-2} \text{h}^{-1}$ )

$\Delta\pi$	—	apparent osmotic pressure difference (bar)
$\Delta\pi_{\text{eff}}$	—	effective osmotic pressure difference (bar)
$K$	—	mass transfer coefficient ( $\text{m s}^{-1}$ )
$\pi_{\text{D,b}}$	—	the bulk osmotic pressure of the DS (bar)
$\pi_{\text{F,m}}$	—	the osmotic pressure at the membrane surface (bar)
$D$	—	diffusion coefficient of the draw solute ( $\text{m}^2 \text{s}^{-1}$ )
$S$	—	membrane structural parameter ( $\mu\text{m}$ )
$\tau$	—	tortuosity
$J_w^t$	—	theoretical water flux ( $\text{L m}^{-2} \text{h}^{-1}$ )
$r$	—	rate of water flux reduced in FO to the membrane theoretical water flux (%)

## References

- [1] C. Charcosset, A review of membrane processes and renewable energies for desalination, *Desalination* 245 (2009) 214–231.
- [2] L.A. Hoover, W.A. Phillip, A. Tiraferri, N.Y. Yip, M. Elimelech, Forward with osmosis: Emerging applications for greater sustainability, *Environ. Sci. Technol.* 45 (2011) 9824–9830.
- [3] J.-J. Qin, W.C.L. Lay, K.A. Kekre, Recent developments and future challenges of forward osmosis for desalination: A review, *Desalin. Water Treat.* 39 (2012) 123–136.
- [4] P. Mondal, A.T.K. Tran, B.V.d. Bruggen, Removal of As(V) from simulated groundwater using forward osmosis: Effect of competing and coexisting solutes, *Desalination* 348 (2014) 33–38.
- [5] P.H.H. Duong, T.-S. Chung, Application of thin film composite membranes with forward osmosis technology for the separation of emulsified oil–water, *J. Membr. Sci.* 452 (2014) 117–126.
- [6] Y. Fang, L. Bian, X. Wang, Understanding membrane parameters of a forward osmosis membrane based on nonequilibrium thermodynamics, *J. Membr. Sci.* 437 (2013) 72–81.
- [7] S. Zhang, K.Y. Wang, T.-S. Chung, H. Chen, Y.C. Jean, G. Amy, Well-constructed cellulose acetate membranes for forward osmosis: Minimized internal concentration polarization with an ultra-thin selective layer, *J. Membr. Sci.* 360 (2010) 522–535.
- [8] J.R. McCutcheon, M. Elimelech, Influence of concentration and dilute internal concentration polarization on flux behavior in forward osmosis, *J. Membr. Sci.* 284 (2006) 237–247.
- [9] C.Y. Tang, Q. She, W.C.L. Lay, R. Wang, R. Field, A.G. Fane, Modeling double-skinned FO membranes, *Desalination* 283 (2011) 178–186.
- [10] G.D. Mehta, S. Loeb, Internal polarization in the porous substructure of a semipermeable membrane under pressure-retarded osmosis, *J. Membr. Sci.* 4 (1978) 261–265.
- [11] B.S. Chanukya, S. Patil, N.K. Rastogi, Influence of concentration polarization on flux behavior in forward osmosis during desalination using ammonium bicarbonate, *Desalination* 312 (2013) 39–44.
- [12] N.Y. Yip, A. Tiraferri, W.A. Phillip, J.D. Schiffman, M. Elimelech, High performance thin-film composite forward osmosis membrane, *Environ. Sci. Technol.* 44 (2010) 3812–3818.
- [13] N. Ma, J. Wei, R. Liao, C.Y. Tang, Zeolite-polyamide thin film nanocomposite membranes: Towards enhanced performance for forward osmosis, *J. Membr. Sci.* 405–406 (2012) 149–157.
- [14] J. Wei, X. Liu, C. Qiu, R. Wang, C.Y. Tang, Influence of monomer concentrations on the performance of polyamide-based thin film composite forward osmosis membranes, *J. Membr. Sci.* 381 (2011) 110–117.
- [15] E.s.t. S. Romero-Vargas Castrillón, X. Lu, D.L. Shaffer, M. Elimelech, Amine enrichment and poly(ethylene glycol) (PEG) surface modification of thin-film composite forward osmosis membranes for organic fouling control, *J. Membr. Sci.* 450 (2014) 331–339.
- [16] K.Y. Wang, R.C. Ong, T.-S. Chung, Double-skinned forward osmosis membranes for reducing internal concentration polarization within the porous sublayer, *Ind. Eng. Chem. Res.* 49 (2010) 4824–4831.
- [17] A. Tiraferri, Y. Kang, E.P. Giannelis, M. Elimelech, Highly hydrophilic thin-film composite forward osmosis membranes functionalized with surface-tailored nanoparticles, *ACS Appl. Mater. Interfaces* 4 (2012) 5044–5053.
- [18] L. Setiawan, R. Wang, K. Li, A.G. Fane, Fabrication of novel poly(amide–imide) forward osmosis hollow fiber membranes with a positively charged nanofiltration-like selective layer, *J. Membr. Sci.* 369 (2011) 196–205.
- [19] N. Ma, J. Wei, S. Qi, Y. Zhao, Y. Gao, C.Y. Tang, Nanocomposite substrates for controlling internal concentration polarization in forward osmosis membranes, *J. Membr. Sci.* 441 (2013) 54–62.
- [20] G. Han, T.-S. Chung, M. Toriida, S. Tamai, Thin-film composite forward osmosis membranes with novel hydrophilic supports for desalination, *J. Membr. Sci.* 423–424 (2012) 543–555.
- [21] X. Li, K.Y. Wang, B. Helmer, T.-S. Chung, Thin-film composite membranes and formation mechanism of thin-film layers on hydrophilic cellulose acetate propionate substrates for forward osmosis processes, *Ind. Eng. Chem. Res.* 51 (2012) 10039–10050.
- [22] D. Emadzadeh, W.J. Lau, T. Matsuura, M. Rahbari-Sisakht, A.F. Ismail, A novel thin film composite forward osmosis membrane prepared from PSf–TiO<sub>2</sub> nanocomposite substrate for water desalination, *Chem. Eng. J.* 237 (2014) 70–80.
- [23] N. Widjojo, T.-S. Chung, M. Weber, C. Maletzko, V. Warzelhan, The role of sulphonated polymer and macrovoid-free structure in the support layer for thin-film composite (TFC) forward osmosis (FO) membranes, *J. Membr. Sci.* 383 (2011) 214–223.
- [24] R.C. Ong, T.-S. Chung, B.J. Helmer, J.S.d. Wit, Novel cellulose esters for forward osmosis membranes, *Ind. Eng. Chem. Res.* 51 (2012) 16135–16145.
- [25] Y.H. Cho, J. Han, S. Han, M.D. Guiver, H.B. Park, Polyamide thin-film composite membranes based on carboxylated polysulfone microporous support membranes for forward osmosis, *J. Membr. Sci.* 445 (2013) 220–227.
- [26] I.-C. Kim, S.-H. Ahn, Y.-S. Jin, B.-S. Kim, Y.-I. Park, J. Jegal, S.-H. Lee, Y.-N. Kwon, H.-W. Rhee, Preparation of newly synthesized forward osmosis membrane, *Desalin. Water Treat.* 51 (2013) 5191–5195.

- [27] W. Li, Y. Gao, C.Y. Tang, Network modeling for studying the effect of support structure on internal concentration polarization during forward osmosis: Model development and theoretical analysis with FEM, *J. Membr. Sci.* 379 (2011) 307–321.
- [28] A. Tiraferri, N.Y. Yip, A.P. Straub, S. Romero-Vargas Castrillon, M. Elimelech, A method for the simultaneous determination of transport and structural parameters of forward osmosis membranes, *J. Membr. Sci.* 444 (2013) 523–538.
- [29] C. Suh, S. Lee, Modeling reverse draw solute flux in forward osmosis with external concentration polarization in both sides of the draw and feed solution, *J. Membr. Sci.* 427 (2013) 365–374.
- [30] M. Park, J.H. Kim, Numerical analysis of spacer impacts on forward osmosis membrane process using concentration polarization index, *J. Membr. Sci.* 427 (2013) 10–20.
- [31] J. Ren, J.R. McCutcheon, A new commercial thin film composite membrane for forward osmosis, *Desalination* 343 (2014) 187–193.
- [32] D. Emadzadeh, W.J. Lau, T. Matsuura, A.F. Ismail, M. Rahbari-Sisakht, Synthesis and characterization of thin film nanocomposite forward osmosis membrane with hydrophilic nanocomposite support to reduce internal concentration polarization, *J. Membr. Sci.* 449 (2014) 74–85.
- [33] G.R. Guillen, Y. Pan, M. Li, E.M.V. Hoek, Preparation and characterization of membranes formed by nonsolvent induced phase separation: A review, *Ind. Eng. Chem. Res.* 50 (2011) 3798–3817.
- [34] M. Tian, C. Qiu, Y. Liao, S. Chou, R. Wang, Preparation of polyamide thin film composite forward osmosis membranes using electrospun polyvinylidene fluoride (PVDF) nanofibers as substrates, *Sep. Purif. Technol.* 118 (2013) 727–736.
- [35] T.Y. Cath, M. Elimelech, J.R. McCutcheon, R.L. McGinnis, A. Achilli, D. Anastasio, A.R. Brady, A.E. Childress, I.V. Farr, N.T. Hancock, J. Lampi, L.D. Nghiem, M. Xie, N.Y. Yip, Standard methodology for evaluating membrane performance in osmotically driven membrane processes, *Desalination* 312 (2013) 31–38.
- [36] D.L. Shaffer, J.R. Werber, H. Jaramillo, S. Lin, M. Elimelech, Forward osmosis: Where are we now? *Desalination* 356 (2015) 271–284.